

Experimental study of gas-liquid mass transfer coupled with chemical reactions by digital holographic interferometry

C. Wylock^{*,a}, S. Dehaeck^a, T. Cartage^b, P. Colinet^a, B. Haut^a

^a*Université Libre de Bruxelles, TIPs Department, 50 av. F.D. Roosevelt CP 165/67, 1050 Brussels, Belgium*

^b*Solvay S.A., rue de Ransbeek 310, 1120 Brussels, Belgium*

Abstract

This work deals with the development of a new experimental tool and an original procedure to study the gas-liquid absorption process coupled with chemical reactions in the liquid phase. This absorption is realized inside a Hele-Shaw cell and digital holographic interferometry is used to visualize the formation and the development of the diffusion layer during the mass transport in the liquid phase in the vicinity of the gas-liquid interface. An image processing code is developed to extract quantitative information from the raw experimental results. The experimental results are compared to a mass transfer model in the liquid phase of the Hele-Shaw cell and some physico-chemical parameters of this model are estimated from this comparison using a non-linear least-square fitting method. The developed procedure is used to study the gaseous CO₂ absorption in NaHCO₃-Na₂CO₃ aqueous solution. Calibration curves are determined and experiments are realized for several couples of NaHCO₃-Na₂CO₃ initial concentrations. The estimated values of the physico-chemical parameters for each experiment are presented and they are compared to the values calculated from correlations found in the literature. A reasonable agreement is observed, which tends to show that the methodology is promising and could be applicable to other systems.

Key words: absorption, mass transfer, chemical reactions, interferometry, mathematical modeling, parametric estimation

*Corresponding author

Email address: cwylock@ulb.ac.be (C. Wylock)

Preprint submitted to Chemical Engineering Science

January 13, 2011

1. Introduction

A lot of chemical engineering processes are based on chemical reaction between a gas and a component in a liquid phase. It is commonly admitted that the global gas-liquid mass transfer rate is controlled by phenomena occurring in layers close to the gas-liquid interface, especially the coupling between the diffusive transport and the chemical reactions in the liquid phase (Bird et al., 2002; Coulson and Richardson, 1999; Danckwerts, 1970; Trambouze and Euzen, 2004). Therefore, a good understanding of these phenomena is required to achieve an optimization of the processes.

Several approaches, such as the two-film theory (Whitman, 1923), the penetration theory (Higbie, 1935) or the surface renewal theory (Danckwerts, 1970), are presented in the literature to model the global mass transfer rate in a gas-liquid contactor. All these approaches are based on mass balance equations in the thin layer of liquid close to the gas-liquid interface. These models are quite well validated by numerous experimental works in several kinds of devices (e.g. falling liquid film, plug-jet reactor, bubble column, . . .). Nevertheless, these are validated generally at the scale of the gas-liquid contactor. There are few articles which present works validating experimentally, at the local scale, the modeling of the phenomena taking place in the vicinity of the gas-liquid interface when the absorption occurs. As mentioned in (Komiya et al., 2008), one of the key steps in improving the understanding of this phenomenon would be to develop a tool enabling a direct visualization of the absorption at the interface and the reaction-diffusion processes in the liquid phase.

The main objective of this work is the development of a new experimental tool and an original procedure to study phenomena occurring during the gas-liquid absorption coupled with chemical reactions in the liquid phase. The concentration variations due to the mass absorption and the chemical reaction can modify the refractive index of the liquid. Therefore, digital holographic interferometry can be used to visualize the formation and the development of the diffusion layer during the mass transport in this liquid close to the gas-liquid interface (Harvey et al., 2005; Komiya et al., 2008; Konstantinov et al., 2003).

The developed procedure is divided into four modules. These are schematically depicted with their interactions in Fig. 1. They are presented succes-

sively in the present paper.

Fig. 1.

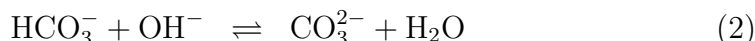
The first module consists of gas-liquid mass absorption experiments. In order to limit the investigation to a two-dimensional situation, these experiments are realized inside a Hele-Shaw cell. A Mach-Zehnder interferometer is then used to visualize the refractive index variations induced by the mass absorption. An image processing code is developed to extract quantitative information from the raw experimental results. The experimental data obtained at this stage contain highly detailed characteristic information on the dynamics of the mass transfer coupled with chemical reactions. In this work, the procedure described in the three following modules is proposed to process these data.

In the second module, a one-dimensional (1-D) mass transfer model is proposed, coupling diffusion and reaction in the liquid phase in the Hele-Shaw cell. This model includes some key physico-chemical parameters (such as solubility, diffusion coefficients, kinetic constants, ...). The accurate determination of these parameters is very important for the modeling of numerous processes including gas-liquid absorption. It is proposed to compare the experimental results to the model simulation results in order to estimate some physico-chemical parameters appearing in this model.

Solving the equations of the model, according to the initial and boundary conditions, enables to simulate the concentration variations as functions of the time and the depth in the liquid from the interface. In order to compare the simulated concentrations with the experimental refractive index, a correlation between concentration and refractive index has to be identified. The third module is therefore devoted to the determination of experimental calibration curves. This calibration is realized by refractometry.

Using the correlation (presented in the third module), the simulated and experimental results can be compared. From this comparison, some physico-chemical parameters of the mass transfer model (developed in the second module) can be estimated from the experimental results (obtained in the first module). These estimations are realized in the fourth module. A parametric estimation method, based on a non-linear least-square fitting, is used to estimate some physico-chemical parameters of the mass transfer model in the Hele-Shaw cell. This method compares the experimental results with the simulated results and estimates the parameters that minimizes the differences between them.

The experimental tool and the procedure presented in this paper are used to study the gaseous CO₂ absorption in NaHCO₃-Na₂CO₃ aqueous solution. This absorption is coupled with the two following chemical reaction in the liquid phase (Cents et al., 2005; Danckwerts, 1970; Haut et al., 2004; Vas Bhat et al., 2000)



This system is well known and characterized in the literature. Correlations can be found for all of the physico-chemical parameters of this system. The results obtained using the procedure described in this paper can be compared to the results obtained in numerous other works. This system is therefore used as a test case. Notice that the study of this absorption is also of industrial interest, since it is realized in several production processes (for instance in the sodium bicarbonate production).

A set of CO₂ absorption experiments, using several couples of NaHCO₃-Na₂CO₃ initial concentrations, are realized. For each experiment, some physico-chemicals parameters of the proposed mass transfer model are then estimated. The estimated values of these parameters are presented and they are compared to the values calculated from correlations found in the literature.

2. Gas-liquid mass absorption experiments

2.1. Experimental setup

The gas-liquid CO₂ absorption process is realized inside a Hele-Shaw cell (see Fig. 2). This cell is made of two transparent flat plates (5 × 10 cm) of polymethyl methacrylate, separated by a narrow distance using a silicone spacer (gap of 1.9 mm, measured using a calliper rule). An aqueous solution of NaHCO₃ and Na₂CO₃ is injected by the bottom of the cell and fills partially the space between the plates. The free interface formed between the gaseous and the liquid phases is horizontal but presents a meniscus.

The CO₂ absorption in this stagnant liquid is then realized by forcing gaseous CO₂ to flow along this interface thanks to the particular shape of the spacer between the two plates, with an obstacle between the gas inlet and outlet (see Fig. 2). This shape is used to ensure a homogeneous and constant CO₂ partial pressure in the gaseous phase above the interface. The

gas flow is set to 1 ml/min and the CO₂ partial pressure above the liquid phase is close to 0.98 bar. At the end of the liquid injection, the gas-liquid interface is placed approximately 1 cm below the bottom of the obstacle.

In order to minimize the evaporation of the aqueous solution, the CO₂ gas flow is saturated with water vapor prior to its entrance into the cell. CO₂ from a gas cylinder is bubbled through demineralised water to saturate the gas before passing it through a mass flow meter after which it is injected in the cell.

All the experiments are performed at room temperature, which is 20 ° C.

Fig. 2.

This Hele-Shaw cell is placed in a Mach-Zehnder interferometer as shown in Fig. 3. The He-Ne laser beam (wavelength $\lambda=632.8$ nm) is expanded and "cleaned" using a spatial filter, before being splitted into a reference beam and an object beam thanks to a beamsplitter. The reference beam passes through the ambient air while the object beam passes through the test cell. Finally, the two beams are recombined at a second beamsplitter and imaged on a CCD camera by a Micro-Nikkor objective with a focal length of 200 mm.

Fig. 3.

As the optical paths of the two beams are different, there is, in general, a non-homogeneous phase difference between them. Therefore, an image presenting interference fringes (hereafter called an interferogram) is observed. The mirror 2 is slightly tilted in order to get a linear phase difference in the horizontal direction. Therefore, even if there is an optical uniformity in the experimental cell, vertical interference fringes are observed in the interferogram. Such a reference interferogram is presented with a diagram of the Hele-Shaw cell in Fig. 4.

Fig. 4.

Each interferogram has 1024×1024 pixels. The calibration of the image size is performed using a Ronchi Ruling by the procedure described by Dehaeck (2007). It is estimated that the observation window size is 7mm×7mm.

The horizontal black strip observed in Fig. 4 corresponds to the gas-liquid interface. Indeed, the meniscus shape of this interface deflects the

object beam light in this zone. Therefore, this zone appears in black in the interferograms.

It is also observed in Fig. 4 that interference fringes have a different orientation in the image part corresponding to the gaseous phase. This effect is related to the significant difference between the refractive indexes of the liquid phase (close to 1.33) and the gaseous phase (close to 1) but it has no influence on the presented procedure since only the liquid phase part of the image is used.

2.2. Experimental protocol

At the initial state, the interference fringes are vertical in the liquid phase, as showed in Fig. 5-a. Before the beginning each experiment, such an interferogram is recorded. It is used as the reference interferogram. As soon as the CO₂ absorption is started, it is observed that the fringes bend in the zone of the image corresponding to the liquid phase just below the interface. An interferogram recorded 15 min after the beginning of the transfer is presented in 5-b. The interferograms are recorded every 2 seconds.

Fig. 5.

The gas-liquid CO₂ absorption induces local concentration variations in the liquid phase, that lead to local refractive index variations compared with the homogeneous initial state. These variations depend on the transfer time and the distance from the interface. Therefore, the optical path of a given ray of the object beam passing through the liquid is modified by the local variation of the refractive index when the absorption has started. It leads to a variation of the phase difference with the corresponding ray in the reference beam reaching the same pixel of the CCD camera. The light intensity on this pixel is then changed. This phase difference variation is called a phase shift.

At the scale of the interferogram, the phase shifts between the reference beam and the object beam lead to a time and space evolution of the fringe positions, which is called fringe bending. By following this fringe bending in the image part corresponding to the liquid phase, this device is an accurate instrument to detect small local variation of the refractive index (Hecht, 1987) during the mass absorption in the liquid. Therefore, this set-up enables to visualize the formation and the time evolution of the diffusion layer with different concentrations of the various chemical species that is formed in the liquid.

Notice that a thickening of the interface region is sometimes observed, as between Figs. 5-a and 5-b. This phenomenon is observed during the onset of the gas flow. The equilibrium state of the meniscus was probably not reached before the beginning of some experiments. A few seconds after the beginning, this equilibrium state is assumed to be reached as it is observed that the meniscus thickness remains stable during the remainder of the experiment after this thickening stage.

Gas-liquid CO₂ absorption experiments are realized for solutions having various concentrations in NaHCO₃ and Na₂CO₃. For each couple of NaHCO₃ and Na₂CO₃ concentrations, two experiments are realized. Each experiment runs 15 min. Beyond this time, chemo-hydrodynamical instabilities are generally observed. These instabilities have been studied in a previous work (Wylock et al., 2008) and, therefore, they are not further presented in this paper.

2.3. Image processing

An image processing code has been developed by Dehaeck et al. (2008) in order to compute the phase shifts in the object beam at a given time from the fringe bending observed on the interferogram at this time. This code is based on the method developed by Takeda et al. (1982) and described by Kreis (1986, 2005).

For each interferogram, the two-dimensional (2-D) Fast Fourier Transform (FFT) is applied. The logarithm of the 2-D FFT of an interferogram in the Fourier space, which is also called power spectrum, is presented in Fig. 6-a in gray level. White zones correspond to a high signal and black zones to a low signal. Three white peaks are especially observed: one at the center of the image, and two at the left and the right side of the center, symmetrically to it. It has been shown (Takeda et al., 1982; William W. Macy, Jr., 1983) that the peaks at the left and the right sides are complex conjugates of the Fourier transform of the object beam. Therefore, one of these two peaks is selected for the following processing. In this work, the right peak is selected.

The image presented in Fig. 6-a is then filtered in order to keep only one peak of the image. The used filter is a rectangle box that is centered at the position of the peak at the right side. Its half-width corresponds to 50% of the distance between the center of the rectangle and the center of the image. The half-height corresponds to 1000% of this distance. The image part outside this box is cut away by replacing the gray level values of the power spectrum by zero.

Finally, the remaining power spectrum is placed at the center of the image. The resulting image is presented in Fig. 6-b, where the remaining power spectrum is in gray level at the central part of the image. The zero values are shown in black.

Fig. 6.

The inverse 2-D FFT then is applied to the image presented in Fig. 6-b. Since the remaining spectrum is no longer symmetrical, it does not belong to a real function in the spatial domain. Therefore, the obtained value at each pixel is a complex number.

The phase of the complex number at each pixel is obtained by applying the inverse tangent at the ratio of the imaginary part on the real part. This phase corresponds to the phase of the light in the object beam.

To get the phase shifts at a given time, the phase field of the reference interferogram (recorded just before the beginning of the absorption), computed also following this procedure, is subtracted from the phase field computed from the interferogram at this time. Let c_{ref} and c_t be the complex numbers obtained at a given pixel from the reference interferogram processing and from the processing of the interferogram at the time t , respectively. The phase shift $\Delta\zeta(t)$ at the time t at this pixel is then calculated by (Kreis, 1986):

$$\Delta\zeta(t) = \arctan\left(\frac{\Re(c_{\text{ref}})\Im(c_t) - \Im(c_{\text{ref}})\Re(c_t)}{\Re(c_{\text{ref}})\Re(c_t) + \Im(c_{\text{ref}})\Im(c_t)}\right) \quad (3)$$

where \Re and \Im denote the real part and the imaginary part, respectively.

The obtained phase shift field is "wrapped", as the value of the phase shift at each pixel is between $-\pi$ and $+\pi$. The resulting field is illustrated in Fig. 7 in gray level, where white zones correspond to $\Delta\zeta = +\pi$ and black zones to $\Delta\zeta = -\pi$. The sharp transition between white and black zone correspond to the transitions of the phase field shift from $+\pi$ to $-\pi$ between successive pixels.

Fig. 7.

The phase shift field is made continuous by two one-dimensional (1-D) unwrapping steps of the phase shift field, which are applied successively. In a first time, the bottom row is unwrapped horizontally, starting from the left and going to the right. In a second time, each column is unwrapped

vertically, starting from the bottom and going up. The method used for the one-dimensional unwrapping is the method proposed by Itoh (1982).

As mentioned previously, the phase shifts in the object beam are related to the refractive index variations in the liquid phase in the cell. Let $\Delta\zeta$ be the phase shift at a given pixel. The corresponding refractive index variation Δn at this pixel is calculated by this equation (Kreis, 2005):

$$\Delta n = \frac{\lambda}{2\pi e} \Delta\zeta \quad (4)$$

where e is the thickness of the liquid traversed by the beam. It corresponds to the gap between the two plates of the cell. A refractive index variation field is presented in Fig. 8.

Fig. 8.

3. Mathematical modeling

In order to analyse the obtained experimental results, a model of the mass transfer in the Hele-Shaw cell is proposed.

During the CO₂ absorption, it is observed in Fig. 5-b that the fringes bend but remain parallel, at least for not too long time (indeed, instabilities eventually appear as mentioned in section 2.2), even when there is a meniscus thickening at the gas flow onset. It means that the liquid refractive index variations are homogeneous in the horizontal direction. A front of refractive index variations penetrates in the liquid following the vertical direction. It can be assumed that the concentration gradients are significant only in the direction perpendicular to the gas-liquid interface. Therefore, the evolution of the observed diffusion layer can be modeled by a 1-D transient equation system for comparing with the experimental results.

Let x be the vertical axis, perpendicular to the interface and pointing towards the liquid phase. x corresponds to the depth in the liquid from the interface. Let t be the time.

As the liquid phase is stationary, the diffusion is the only mass transfer mechanism. This diffusion process is coupled with chemical reactions in the liquid phase, induced by the CO₂ gas-liquid transfer. Since OH⁻, HCO₃⁻ and CO₃²⁻ are ions, their motions induce an electric field which can alter the diffusion process. Nevertheless, preliminary simulations have been realized using Nernst-Planck equations and they have shown that it does not have

important effects on the simulated concentration profiles. On the other hand, it increases considerably the computation time. Therefore, a simple 1-D diffusion-reaction model, such the one presented in (Vas Bhat et al., 2000), can be used.

A non-dimensionalization of the governing equations of this latter model has been realized, in order to stress the significance of some physico-chemical parameters. They can be estimated using the correlations presented in Appendix. In the case of the CO₂ absorption in NaHCO₃/Na₂CO₃ solution and for the concentration ranges studied in this work, some of them take very large values, suggesting simplifications of the model. It appears that it is not necessary to take into account the diffusion-reaction equation for OH⁻ and that the reaction (2) is always at equilibrium. The OH⁻ concentration can be then evaluated using the HCO₃⁻ and CO₃²⁻ concentrations and the equilibrium constant of (2). Moreover, the reaction (1) can be considered as irreversible. Therefore, the reactions (1) and (2) can be simplified by this global reaction:



The reaction rate r is calculated as follows:

$$r = k_{11} [\text{CO}_2] \frac{[\text{CO}_3^{2-}]}{K_2 [\text{HCO}_3^-]} \quad (6)$$

where k_{11} is the kinetic constant of the reaction (1) and K_2 is the equilibrium constant of the reaction (2).

The diffusion-reaction equations of the model proposed in this work to compare with experimental results read therefore:

$$\frac{\partial [\text{CO}_2]}{\partial t} = D_{\text{CO}_2} \frac{\partial^2 [\text{CO}_2]}{\partial x^2} - r \quad (7)$$

$$\frac{\partial [\text{HCO}_3^-]}{\partial t} = D_{\text{HCO}_3^-} \frac{\partial^2 [\text{HCO}_3^-]}{\partial x^2} + 2r \quad (8)$$

$$\frac{\partial [\text{CO}_3^{2-}]}{\partial t} = D_{\text{CO}_3^{2-}} \frac{\partial^2 [\text{CO}_3^{2-}]}{\partial x^2} - r \quad (9)$$

D_{CO_2} , $D_{\text{HCO}_3^-}$ and $D_{\text{CO}_3^{2-}}$ are the diffusion coefficient of CO₂, HCO₃⁻ and CO₃²⁻, respectively. They can be estimated using the correlations presented in Appendix. Notice that the correlations proposed for HCO₃⁻ and CO₃²⁻ lead to rough estimations of $D_{\text{HCO}_3^-}$ and $D_{\text{CO}_3^{2-}}$ since they are valid for infinitely dilute solutions.

Let $[\text{CO}_2]_0$, $[\text{HCO}_3^-]_0$ and $[\text{CO}_3^{2-}]_0$ be the initial concentrations in the liquid phase, before the beginning of the CO_2 absorption. The initial conditions write:

$$\begin{aligned} [\text{CO}_2]_{|x,t=0} &= [\text{CO}_2]_0 \quad , \\ [\text{HCO}_3^-]_{|x,t=0} &= [\text{HCO}_3^-]_0 \quad , \quad [\text{CO}_3^{2-}]_{|x,t=0} = [\text{CO}_3^{2-}]_0 \end{aligned} \quad (10)$$

At the interface ($x=0$), the interfacial CO_2 concentration in the liquid phase is assumed to be instantaneously at equilibrium with the gaseous phase (Harvey and Smith, 1959). The other species do not pass through the interface. Therefore, the boundary conditions at the interface write

$$\begin{aligned} [\text{CO}_2]_{|x=0,t} &= h \frac{p_{\text{CO}_2}}{RT} \quad , \\ \frac{\partial [\text{HCO}_3^-]}{\partial x} \Big|_{x=0,t} &= 0 \quad , \quad \frac{\partial [\text{CO}_3^{2-}]}{\partial x} \Big|_{x=0,t} = 0 \end{aligned} \quad (11)$$

where h is the CO_2 solubility coefficient, p_{CO_2} is the CO_2 partial pressure in the gaseous phase, R is the perfect gas constant and T is the absolute temperature. h can be estimated using the correlation presented in Appendix.

Far from the interface (for $x \rightarrow \infty$), the concentrations are assumed to correspond to the initial homogeneous concentrations. Therefore, the conditions far from the interface write

$$\begin{aligned} \lim_{x \rightarrow \infty} \frac{\partial [\text{CO}_2]}{\partial x} \Big|_{x,t} &= 0 \quad , \\ \lim_{x \rightarrow \infty} \frac{\partial [\text{HCO}_3^-]}{\partial x} \Big|_{x,t} &= 0 \quad , \quad \lim_{x \rightarrow \infty} \frac{\partial [\text{CO}_3^{2-}]}{\partial x} \Big|_{x,t} = 0 \end{aligned} \quad (12)$$

The boundary-value problem is solved numerically by a finite element method. The 1-D diffusion mode of the chemical engineering module of the COMSOL Multiphysics 3.4 software is used. The 1-D computational domain size is 1 cm. A homogeneous mesh is used and the mesh size is 1 μm . The quadratic Lagrangian element scheme is selected. The equations are solved with the UMFPAK solver.

The numerical resolution enables to determine the space and time concentrations evolution of each species. The graphical representation of a species concentration at a given time as a function of the depth in the liquid is called

the concentration profile at this time. The dimensionless simulated concentration profiles of CO_2 , HCO_3^- and CO_3^{2-} at $t = 15$ min are presented in Fig. 9. The CO_2 concentration is normalized by its concentration at the interface. For the other species, the concentration is normalized by the bulk concentration.

Fig. 9.

Notice that, for a given simulation, the values of the parameters appearing in the mass transfer model are estimated for the considered initial NaHCO_3 and Na_2CO_3 concentrations. No dependence with respect to the space and time evolutions of the concentrations is considered in this model. Therefore, the fitted values of these parameters (see section 7) can be seen as effective values.

4. Calibration

In order to make comparable the simulated concentrations profiles with the experimental refractive index variation fields, correlations between concentrations variations and refractive index variations have to be identified.

Several solutions, with various concentrations in NaHCO_3 and Na_2CO_3 , are prepared. For each solution, the mass of the dissolved NaHCO_3 and Na_2CO_3 is measured using a precision balance. The resulting concentrations are calculated using the sodium mass balance equation, the carbon mass balance equation, the electro neutrality equation and the equilibrium equations of reactions (1) and (2). The equilibrium constants K_1 and K_2 are estimated using the correlations (34) and (36) presented in Appendix. The density of the solution is measured using a densimeter Anton Paar DMA 4500 and its refractive index is measured with an Abbe refractometer ATAGO DR-A1. All the measurement are realized at 20°C .

The calibration procedure is realized in two steps.

On the one hand, the refractive index of each solution is plotted versus its density. The results are presented in Fig. 10.

Fig. 10.

It is observed that the refractive index of the liquid grows linearly with its density. Therefore, the following equation can be written

$$\Delta n = \frac{\partial n}{\partial \rho} \Delta \rho \quad (13)$$

where Δn is the refractive index variation induced by the density variation $\Delta\rho$.

The numerical value of $\frac{\partial n}{\partial\rho}$ can be estimated by the slope of the linear trend line of these point. The result is

$$\frac{\partial n}{\partial\rho} = 0.2056 \frac{\text{m}^3}{\text{kg}} \quad (14)$$

with a linear regression coefficient equals to 0.9951.

The refractive index variation fields determined by the interferograms processing can be therefore converted into density variation fields using Eq. 13. A window of averaging is defined on this density variation field, as shown in Fig. 11-a. For each horizontal line in this window, the density variations are averaged.

The graphical representation of the averaged density variations, at a given time, plotted versus the distance from the interface is called the density variation profile at this time. This procedure is applied for each density variation field. The density variation profiles at each time are then obtained. Some density variation profiles, from $t=0\text{s}$ to $t=400\text{s}$, are presented in Fig 11-b.

Fig. 11.

On the other hand, the experimental density variation profiles cannot be directly compared to the simulation results, as the relation between the density and the concentrations is not univocal. Several couples of NaHCO_3 - Na_2CO_3 concentrations can have the same density. Therefore, the simulated concentration profiles, obtained from the numerical resolution of the mass transfer model, have to be converted into density variations profiles in order to compare with the experimental density variation profiles.

In a first stage, the density of each solution is plotted versus its estimated HCO_3^- concentration in Fig. 12. The set of experimental points consists in three subsets, depicted by the squares, the circles and the diamonds. The solutions in each subset have approximately the same CO_3^{2-} concentration.

Fig. 12.

In a second stage, the density of each solution is plotted versus its estimated CO_3^{2-} concentration in Fig. 13. The set of experimental points

consists in three subsets, depicted by the squares, the circles and the diamonds. The solutions in each subset have approximately the same HCO_3^- concentration.

Fig. 13.

From the calibration measurements, it is therefore observed that the density variations are mainly due to the HCO_3^- and the CO_3^{2-} concentration variations. Moreover, the CO_2 and OH^- concentrations are four order of magnitude less than the HCO_3^- and the CO_3^{2-} concentrations. The following equation is then proposed:

$$\Delta\rho = \frac{\partial\rho}{\partial[\text{HCO}_3^-]}\Delta[\text{HCO}_3^-] + \frac{\partial\rho}{\partial[\text{CO}_3^{2-}]}\Delta[\text{CO}_3^{2-}] \quad (15)$$

where $\Delta[\text{HCO}_3^-]$ and $\Delta[\text{CO}_3^{2-}]$ are the concentration variations of the HCO_3^- and the CO_3^{2-} compared to their initial concentration, respectively. They are calculated from the HCO_3^- and the CO_3^{2-} concentration profiles, respectively:

$$\Delta[\text{HCO}_3^-](x, t) = [\text{HCO}_3^-](x, t) - [\text{HCO}_3^-]_0 \quad (16)$$

$$\Delta[\text{CO}_3^{2-}](x, t) = [\text{CO}_3^{2-}](x, t) - [\text{CO}_3^{2-}]_0 \quad (17)$$

The numerical value of $\frac{\partial\rho}{\partial[\text{HCO}_3^-]}$ is estimated by averaging the slopes of the 3 linear trend lines presented in Fig. 12 and the value of $\frac{\partial\rho}{\partial[\text{CO}_3^{2-}]}$ is estimated by averaging the slopes of the three linear trend lines presented in Fig. 13. The following values are obtained:

$$\frac{\partial\rho}{\partial[\text{HCO}_3^-]} = 0.057 \pm 0.003 \frac{\text{kg}}{\text{mol}} \quad (18)$$

$$\frac{\partial\rho}{\partial[\text{CO}_3^{2-}]} = 0.099 \pm 0.006 \frac{\text{kg}}{\text{mol}} \quad (19)$$

From the simulated concentration profiles, the simulated density variation profiles can be calculated using Eqs. (15), (16) and (17). The simulated density variation profiles, calculated from the simulated concentration profiles presented in Fig. 9, are presented in Fig. 14.

Fig. 14.

5. Preliminary analysis

Before analyzing the experimental results, it has to be verified that some characteristics of the studied system, such as the potential effects of the heat of absorption and reaction, the presence of the meniscus or the gas flow, do not affect significantly the mass transfer mechanism and, therefore, do not invalidate the proposed procedure.

A preliminary analysis is realized in order to check that these characteristics are not problematic for our particular studied system. It is important to notice that this analysis is not general and should be repeated for other systems.

5.1. Thermal effects

The gas-liquid CO₂ absorption and chemical reactions induced by this absorption are slightly exothermic. As temperature variations can also induce refractive index variations, the absorption thermal effects are evaluated by numerical simulations.

In pure water, the refractive index variation due to temperature variation can be estimated by :

$$\frac{dn}{dT} = -0.985 \cdot 10^{-4} \text{ K}^{-1} \quad (20)$$

for the wavelength $\lambda = 632.8 \text{ nm}$ (Kreis, 2005).

The heat transport equation is coupled to the boundary-value problem given by Eqs. (7)-(12):

$$\rho c_p \frac{\partial T}{\partial t} + k \frac{\partial^2 T}{\partial x^2} = Q \quad (21)$$

where ρ , c_p and k are the density, the specific heat capacity and the thermal conductivity, respectively. It is assumed that the thermal properties of NaHCO₃/Na₂CO₃ solutions are close to those of pure water. Therefore, the values for pure water are used.

Q denotes the heat production due to the chemical reactions. It reads:

$$Q = -r (\Delta H_{r_1} - \Delta H_{r_2}) \quad (22)$$

The numerical values of the enthalpy of reactions (1) and (2), $\Delta H_{r_1} = -46.024 \text{ kJ/mol}$ and $\Delta H_{r_2} = -20.3 \text{ kJ/mol}$ respectively, are found in (Planck,

1903). A heat flux is assumed at the interface due to the CO₂ absorption. The boundary condition at $x = 0$ reads:

$$k \left. \frac{\partial T}{\partial x} \right|_{x=0,t} = \Delta H_{\text{abs}} D_{\text{CO}_2} \left. \frac{\partial [\text{CO}_2]}{\partial x} \right|_{x=0,t} \quad (23)$$

Far from the interface, it is assumed that the heat flux equals 0. The boundary condition for $x \rightarrow \infty$ reads:

$$\lim_{x \rightarrow \infty} \left. \frac{\partial T}{\partial x} \right|_{x,t} = 0 \quad (24)$$

From the simulation results, it is estimated that the temperature gradient is quite small. Since the thermal conductivity is much larger than the mass diffusivity, the thermal layer is much larger than the diffusion layer. The temperature increase is almost homogeneous in the observation window. Moreover, this temperature increase is quite limited. It is evaluated to 0.21 K near the interface after 15 min. It corresponds to a refractive index decrease of 10^{-5} , using Eq. (20). This variation is one order of magnitude below the variations due to the mass transfer and chemical reactions.

Therefore, it is considered that thermal effects can be neglected.

5.2. Gas flow effects

It has been verified that the gas flow does not trigger interfacial liquid motion induced by shear stresses and instabilities induced by water evaporation. Indeed, water evaporation would lead to a temperature decrease due to the latent heat, inducing small refractive variations at the interface and an increase of the water density. This latter could lead to the apparition of instabilities.

The experimental protocol was applied to demineralised water only and the interface region was observed for 2 hours. No liquid motion or refractive index variations have been observed during the test experiment. Moreover, the position of the interface has not changed after 2 h.

Therefore, it is confirmed that there is no interfacial motion induced the gas flow and there are no refractive index perturbations neither instabilities induced by residual water evaporation.

5.3. Meniscus shape

The effect of the meniscus shape on the mass transfer has been estimated by a numerical simulation of the boundary-value problem given by Eqs. (7)-(12) in a two-dimensional domain corresponding to a vertical cross-section of the cell, in the perpendicular direction to the plates.

From this simulation, it has been estimated that the liquid phase in the meniscus region is quickly saturated. The concentrations in the horizontal liquid layers below the meniscus are quasi homogeneous.

Therefore, it can reasonably be assumed that the liquid traversed by each given ray of the object beam (in the horizontal direction perpendicular to the plates) is homogeneous.

6. Physico-chemical parameter estimation

One of the main objectives of the procedure presented in this paper is to compare mass transfer experimental data with a mathematical model, in this case by the comparison of experimental density variation profiles with profiles obtained from simulation of the mass transfer model. This model contains physico-chemical parameters and a numerical value has to be given to each one to simulate the model.

For the studied system (CO_2 in aqueous solution of NaHCO_3 and Na_2CO_3), the values of the physico-chemical parameters are estimated by the correlations presented in Appendix and by Eqs. (18) and (19). It is observed that, when these values are used to compute the simulated profiles, these latter profiles do not agree with the experimental ones, as presented in Fig. 15.

Fig. 15.

This result tends to show that some parameters of the model are not estimated with a sufficient accuracy, regarding to the model sensitivity with respect to these parameters. Indeed, the proposed model has eight physico-chemical parameters, but the sensitivity of these profiles with respect to them can be variable.

A parametric sensitivity analysis is realized in order to identify the parameters toward which these profiles are the most sensitive and to classify them. A parametric estimation method is then used to fit some physico-chemical parameters of the mass transfer model from the experimentally observed density variation profiles, in order to reach an agreement between experiments and simulations.

6.1. Selection of the parameters

The parametric sensitivity analysis shows that the simulated density profiles are moderately sensitive to D_{CO_2} , h , k_{11} and K_2 , strongly sensitive to $D_{\text{HCO}_3^-}$ and $D_{\text{CO}_3^{2-}}$, and very strongly sensitive to $\frac{\partial \rho}{\partial [\text{HCO}_3^-]}$ and $\frac{\partial \rho}{\partial [\text{CO}_3^{2-}]}$ (Wylock, 2009).

As a consequence, it is observed that four parameters have necessarily to be fitted to reach an agreement between simulated and experimental density variation profiles: $\frac{\partial \rho}{\partial [\text{HCO}_3^-]}$, $\frac{\partial \rho}{\partial [\text{CO}_3^{2-}]}$, $D_{\text{HCO}_3^-}$ and $D_{\text{CO}_3^{2-}}$. It follows logically from the fact that the density variation profiles depend strongly on the time evolution of the HCO_3^- and CO_3^{2-} concentration profiles. Moreover, it appears that the correlations used for the (rough) estimations of $D_{\text{HCO}_3^-}$ and $D_{\text{CO}_3^{2-}}$, and the experimental correlations for $\frac{\partial \rho}{\partial [\text{HCO}_3^-]}$ and $\frac{\partial \rho}{\partial [\text{CO}_3^{2-}]}$ (Eqs. (18) and (19), which have approximately 5% of precision) are not accurate enough to reach an agreement (such as in Fig. 15). Therefore, these four parameters are always included in the parametric estimation.

It is observed that k_{11} , h and K_2 can also be included in the parametric estimation procedure, since the density variation profiles are sensitive enough to them. For D_{CO_2} , the sensitivity is not enough to reach reliable results.

6.2. Parametric estimation method

Some physico-chemical parameters of the mass transfer model are estimated using a non-linear quadratic fitting method (Walter and Pronzato, 1997). This method estimates the values of the parameters which minimize the differences between the simulated density variation profiles and the experimental ones.

Let $\Delta \rho_{\text{exp}}(t_j, x_i)$ be the experimental density variation at the time t_j and at the distance x_i from the interface. For a set of parameters P , let $\Delta \rho_{\text{sim}}(t_j, x_i, P)$ be the simulated density variation computed at this time t_j at this position x_i .

The cost function C_F is defined as the sum of the squares of the differences between the experimental and the simulated density variation for each x_i and t_j . It is expressed as follows:

$$C_F(P) = \sum_j \sum_i (\Delta \rho_{\text{exp}}(t_j, x_i) - \Delta \rho_{\text{sim}}(t_j, x_i, P))^2 \quad (25)$$

The minimization of the cost function is achieved using the *fminsearch* routine in a COMSOL script of COMSOL Multiphysics. Starting from ini-

tial guesses of the parameters, the script computes the concentration profiles, converts them into density variation profiles and compute the cost function. The *fminsearch* routine changes iteratively the values of the parameters included in the parameter set P in order to decrease the value of the cost function, until it minimizes the cost function. Notice that only the parameters included in P are allowed to be changed through the iterative process. The other parameters remain constant.

The parameter values estimated from the correlations presented in Appendix and from Eqs. (18) and (19) are used as initial guesses. The parameters estimated by the parametric estimation procedure are called the fitted parameters.

7. Results and discussion

The described procedure is applied for several $\text{NaHCO}_3\text{-Na}_2\text{CO}_3$ aqueous solutions.

In a first stage, only the “base” parameters are estimated by the fitting procedure. These are the parameters identified as those with respect to which the simulated density variation profiles are the most sensitive. In a second stage, some other parameters, with respect to which the simulated profiles are sensitive enough, are also included in the parametric estimation. In all cases, the obtained values can be compared to the correlations to discuss the relevance of the results.

7.1. Estimation of the base parameters

The parametric fitting procedure is used to estimate the numerical values of $D_{\text{HCO}_3^-}$, $D_{\text{CO}_3^{2-}}$, $\frac{\partial \rho}{\partial [\text{HCO}_3^-]}$ and $\frac{\partial \rho}{\partial [\text{CO}_3^{2-}]}$, since the density variation profiles are the most sensitive with respect to these parameters. The other parameter values (D_{CO_2} , h , k_{11} and K_2) are estimated by the correlations presented in Appendix and remain constant during the fitting procedure. The fitted parameter values are presented in Table 1.

Table 1.

When the simulated density variation profiles are computed with the fitted parameters values and are compared to the experimental density variation profiles, a good agreement is observed for all cases. An example of density variation profiles comparison, with fitted parameters, is presented in Fig. 16.

However, it is observed that the simulated profiles, especially for the smallest times and sometimes for the largest times, deviate from the experimental ones, especially in the zone close to the interface.

Fig. 16.

This difference comes most probably from the hypothesis that *all* the physico-chemical parameters of the mass transfer model in the Hele-Shaw cell are constant. When the parameter fitting is achieved, each parameter is assumed to remain constant in time and space but some physico-chemical parameters depend on the concentration. As the concentrations vary in the vicinity of the interface, these physico-chemical parameters are expected to be modified, such as the effective diffusion coefficient of HCO_3^- and CO_3^{2-} due to the electric field induced by the ion flows.

The parametric estimation procedure enables to find the set of parameters which minimizes globally the cost function. Therefore, the obtained fitted parameter value corresponds to intermediate or average values, in some sense.

It is observed that the $D_{\text{HCO}_3^-}$ and $D_{\text{CO}_3^{2-}}$ fitted values can vary strongly from one experience to another. This results could be expected since they are likely to depend on the concentrations and the literature correlations are valid only for infinitely dilute solutions. Nevertheless, all these fitted values are in the range $[10^{-10}; 10^{-9}]$, which is physically consistent.

Concerning the fitted values of $\frac{\partial \rho}{\partial [\text{HCO}_3^-]}$ and $\frac{\partial \rho}{\partial [\text{CO}_3^{2-}]}$ presented in Table 1, it is interesting to observe that these values are statistically very similar to the values obtained by the calibration (see Eqs. (18) and (19)). Indeed, the means of $\frac{\partial \rho}{\partial [\text{HCO}_3^-]}$ and $\frac{\partial \rho}{\partial [\text{CO}_3^{2-}]}$ equal 0.055 and 0.111, respectively, with standard deviations of 0.003 and 0.006, respectively.

7.2. Estimation of some other parameters

The parametric fitting procedure is used also to estimate simultaneously the base parameters and h , k_{11} and K_2 , since the density variation profiles are sensitive enough with respect to these three last parameters. The value of D_{CO_2} is estimated by the correlation and remains constant during the fitting procedure.

An example comparison between experimental and simulated density variation profiles, computed with fitted values of $D_{\text{HCO}_3^-}$, $D_{\text{CO}_3^{2-}}$, $\frac{\partial \rho}{\partial [\text{HCO}_3^-]}$, $\frac{\partial \rho}{\partial [\text{CO}_3^{2-}]}$, k_{11} , h and K_2 is presented in Fig. 17. A good agreement is observed. For this case, the following values have been obtained: $k_{11} = 12.5 \text{ m}^3/(\text{mol s})$,

$h = 0.41$ and $K_2 = 5.03 \text{ m}^3/\text{mol}$. These values are consistent with those obtained using the correlations presented in Appendix, since their relative differences are of -2.5%, -1.7% and -8.3%, respectively.

Fig. 17.

The fitted values of h , k_{11} and K_2 for all the experiments are presented in Table 2. For the sake of simplicity, the fitted values of the base parameters are not presented since they are not significantly different from those presented in Table 1.

Table 2.

It is observed in Table 2 that the fitted values of h and k_{11} vary significantly with the initial NaHCO_3 and Na_2CO_3 concentrations. This behavior was expected since it is commonly admitted that these two parameters are influenced by the ion concentrations (see Eqs. (28) and (37) in the appendix, respectively).

The fitted values of h , k_{11} and K_2 are compared to the values obtained using the literature correlations for the whole experimental set. It is observed that the fitted values of k_{11} and h are generally similar to the values estimated with the literature correlations. In average, the relative differences are of -0.6% and -5.3%, respectively, with standard deviations of 3.1% and 7.7%, respectively. For K_2 , the fitted values are also similar to those estimated with the correlation but the variations are generally larger than those for k_{11} and h . In average, the relative differences are of +11.7% with a standard deviation of 11.1%.

These results tend therefore to show that the experimental tool and the procedure proposed in this paper enable to estimate (at least roughly) some important physico-chemical parameters of the mass transfer process.

8. Conclusion and perspectives

This paper presents a new experimental tool and a procedure to estimate some physico-chemical parameters of gas-liquid mass absorption coupled with chemical reactions. The studied case is the absorption of CO_2 in aqueous solutions of NaHCO_3 and Na_2CO_3 . This absorption is realized inside a Hele-Shaw cell, installed in the object beam of a Mach-Zehnder interferometer.

The CO₂ absorption leads to chemical reactions and the subsequent variations of concentrations in the liquid phase induces refractive index variations of the liquid below the interface. An image processing code is developed in order to extract the refractive index variation field in the liquid phase from the interferograms obtained with the interferometer.

The absorption of CO₂, coupled with chemical reaction in the liquid phase, is modelled by a 1-D transient diffusion-reaction model. This model is proposed to simulate the phenomena taking place in the liquid in the Hele-Shaw cell during the mass transfer and to compare with the experimental results, in order to confirm the potential of the experimental tool and the procedure presented in this paper to study mass transfer processes. The equation system of this model is solved numerically and the resolution enables to compute the species concentration profiles in the layer of liquid close to the interface in the Hele-Shaw cell.

In order to make comparable the experimental and the simulated results, calibration curves are determined. On the one hand, it enables to convert the refractive index variation fields obtained from the image processing into liquid density variation fields, which are averaged horizontally to obtain experimental density variation profiles. On the other hand, it enables to convert the numerically determined concentration profiles into simulated density variation profiles.

A set of CO₂ gas-liquid absorption experiments is then realized, for several couples of NaHCO₃ and Na₂CO₃ concentrations. For each experiment in the Hele-Shaw cell, an estimation of the physico-chemical parameters toward which the simulated density variation profiles are the most sensitive ($D_{\text{HCO}_3^-}$, $D_{\text{CO}_3^{2-}}$, $\frac{\partial \rho}{\partial [\text{HCO}_3^-]}$, $\frac{\partial \rho}{\partial [\text{CO}_3^{2-}]}$) is realized. They are identified by a parametric sensitivity analysis. The parametric estimation is realized by comparing the numerically calculated density variation profiles with the experimental ones. A cost function, quantifying the global quadratic differences between the experimental and the simulated profiles, is defined. The parametric estimation is achieved by minimizing this cost function.

Globally, a reasonable agreement is observed between the simulated density variation profiles, generated using the fitted values of the parameters, and the experimental profiles. However, discrepancies can be observed, especially for the smallest times and sometimes for the largest times: the simulated profiles do not agree very well with the experimental ones at the corresponding times, especially in the zone close to the interface. This dif-

ference comes probably from the hypothesis that the fitted parameters are constants, whereas some of these parameters are probably varying during the CO₂ absorption.

Moreover, the parametric estimation procedure can be used as well to fit other physico-chemical parameters if the sensitivity of the simulated density variation profiles with respect to these parameters is sufficient. This is the case for k_{11} , h and K_2 . When these parameters are included in the parametric estimation, the fitted values are globally in reasonable agreement with the values obtained using literature correlations.

Therefore, although discrepancies between experiments and modeling are observed, the results obtained in this work are very promising. They tend to show that the digital holographic interferometry is a powerful tool to study the gas-liquid mass absorption by the visualization of the phenomena occurring in the vicinity of the interface, especially the development of the diffusion layer.

Some improvements of the model and of the parametric estimation method have to be made. For instance, the ion transport equations could be improved using Nernst-Planck or Maxwell-Stefan equations and a maximum likelihood approach could be used instead a least-square method for the parametric estimation. Notice that, for the system studied in this work, it has been estimated that the meniscus shape of the gas-liquid interface does not have an influence on the mass transfer but this is not the case in general. So it would be interesting to get rid of this meniscus, which should be possible by applying a non-wetting coating on the plates above the interface level. Therefore, further investigations will be realized.

Nevertheless, the results obtained in this work tend to confirm the potential of the presented experimental tool and procedure to study mass transfer processes. Besides, the parametric estimation method enables to estimate (at least roughly) simultaneously several important physico-chemical parameters. Therefore, they will be applied to the study of other systems.

Appendix. Physico-chemical parameters

Density and viscosity

The density of the solution, ρ , and the viscosity, μ , are function of the brine composition. They are calculated from correlations provided by Solvay.

CO₂ solubility

The CO₂ solubility in the solution is represented by h . It is the CO₂ concentration ratio between liquid and gaseous phase, when the interface is in the chemical equilibrium state :

$$h = \frac{[\text{CO}_2]_{\text{int}}}{p_{\text{CO}_2, \text{int}}} RT \quad (26)$$

with $[\text{CO}_2]_{\text{int}}$ the CO₂ concentration at the interface in the liquid phase and $p_{\text{CO}_2, \text{int}}$ the pressure of CO₂ at the interface in the gaseous phase.

In pure water, $h = h_w$, and it is estimated by the following expression (Vas Bhat et al., 2000):

$$h_w = 3.59 \cdot 10^{-7} RT \exp\left(\frac{2044}{T}\right) \quad (27)$$

The CO₂ solubility is affected by the presence of ions. The solubility decreases if the ion concentration increases. In the presence of ions, h is calculated by (Pohorecki and Moniuk, 1988; Schumpe, 1993; Vas Bhat et al., 2000; Taghizadeh et al., 2001):

$$\log \frac{h_w}{h} = \left(9.88 \cdot 10^{-5} [\text{Na}^+] + 5.73 \cdot 10^{-5} [\text{OH}^-] \right. \\ \left. + 1.189 \cdot 10^{-4} [\text{HCO}_3^-] + 1.483 \cdot 10^{-4} [\text{CO}_3^{2-}] \right) \quad (28)$$

Diffusion coefficients

The diffusion coefficient of CO₂ is obtained from (Pohorecki and Moniuk, 1988):

$$D_{\text{CO}_2} = D_{\text{CO}_2, w} \frac{\mu_w}{\mu} \quad (29)$$

where μ_w is the viscosity of pure water.

The CO₂ diffusion coefficient in pure water, $D_{\text{CO}_2, w}$, is calculated by :

$$\log D_{\text{CO}_2, w} = -8.1764 + \frac{712.52}{T} - \frac{259070}{T^2} \quad (30)$$

The diffusion coefficients of the other species are estimated using the following correlations (Vas Bhat et al., 2000) :

$$D_{\text{OH}^-} = \left(-0.1925 + 1.2291\sqrt{T} \right) 10^{-3} \frac{RT}{F^2} \quad (31)$$

$$D_{\text{HCO}_3^-} = 4.45 \cdot 10^{-3} \frac{RT}{F^2} \quad (32)$$

$$D_{\text{CO}_3^{2-}} = \left(3.11 \cdot 10^{-5} + 2.63 \cdot 10^{-10} (T)^3 \right) \frac{RT}{2 F^2} \quad (33)$$

where F is the Faraday constant.

Equilibrium constants

The equilibrium constant of the reaction 1, K_1 , is a function of the temperature and the density of the solution. It is calculated using (Edwards et al., 1978):

$$K_1 = \frac{1}{K_w} \exp \left(\frac{-12092.1}{T} - 36.786 \ln(T) + 235.482 \right) \rho_w \quad (34)$$

where ρ_w is the density of pure water and K_w is the ionic product of water.

K_w is calculated by (Vas Bhat et al., 2000):

$$K_w = 10^{-\left(\frac{5839.5}{T} + 22.4773 \log(T) - 61.2062\right)} \rho_w^2 \quad (35)$$

The equilibrium constant of the reaction 2, K_2 , is a function of the temperature, the density and the ionic strength of the solution. A correlation taking into account the ionic strength is available in the literature (Vas Bhat et al., 2000). However, other works have shown that it leads to an underestimation of K_2 (Cents et al., 2005). In this work, the value of K_2 at infinite dilution is used :

$$\log K_2 = \left(\frac{1568.924}{T} - 2.5865 - 6.737 \cdot 10^{-3} T \right) \quad (36)$$

Kinetic constants

The kinetic constant of the forward reaction 1, k_{11} , is calculated with the following expression (Pohorecki and Moniuk, 1988; Taghizadeh et al., 2001; Aroonwilas et al., 2003):

$$\begin{aligned} \log k_{11} = & \left(8.916 - \frac{2382}{T} \right) \\ & + \left(6 \cdot 10^{-5} [\text{Na}^+] + 1.1 \cdot 10^{-4} [\text{OH}^-] + 1.7 \cdot 10^{-4} [\text{CO}_3^{2-}] \right) \end{aligned} \quad (37)$$

Since reaction 2 involves proton transfer, it is extremely faster than reaction 1. The value of the kinetic constant of the forward reaction 2, k_{21} , is not known accurately. A value of $10^7 \text{ m}^3\text{mol}^{-1}\text{s}^{-1}$ is mentioned in (Vas Bhat et al., 2000).

Acknowledgements

F.R.S.-FNRS(Belgian National Fund for Scientific Research) research fellow Christophe Wylock and research associate Pierre Colinet gratefully acknowledge the financial support from the fund. The authors acknowledge Prof. Delplancke and her team for the density measurements. Part of this research was also funded by the CIMEX-PRODEX Programme managed by the European Space Agency in collaboration with the Belgian Federal Science Policy Office, and by the ARCHIMEDES (ARC 04/09-308) project funded by the Communauté Française de Belgique. Some of the authors would like to acknowledge the travel support of the MULTIFLOW FP7-ITN Network, which has enabled interesting discussions to take place with Prof. S. Kalliadasis (Imperial College London).

References

- Aroonwilas, A., Chakma, A., Tontiwachwuthikul, P., Veawab, A., 2003. Mathematical modelling of mass-transfer and hydrodynamics in CO₂ absorbers packed with structured packing. *Chemical Engineering Science* 58 (17), 4037–4053.
- Bird, R., Stewart, W., Lightfoot, E., 2002. *Transport Phenomena*. John Wiley&Sons, New York.
- Cents, A., Brilman, D., Versteeg, G., 2005. CO₂ absorption in carbonate/bicarbonate solutions: The danckwerts-criterion revisited. *Chemical Engineering Science* 60, 5830–5835.
- Coulson, J., Richardson, J., 1999. *Chemical Engineering Vol. 1 : Fluid flow, heat transfer and mass transfer*, 6th Edition. Butterworth Heinemann.
- Danckwerts, P., 1970. *Gas-Liquid Reactions*. Chemical Engineering Series. McGraw-Hill.

- Dehaeck, S., 2007. Development of glare point, shadow and interferometric planar techniques for gas bubble sizing. Ph.D. thesis, University of Ghent.
- Dehaeck, S., Wylock, C., Colinet, P., 2008. A Mach-Zehnder interferometer-based study of evaporation of binary mixtures in Hele-Shaw cells. In: Proceeding of the 13th International Symposium on Flow Visualisation ISFV 13 - FLUVISU 12. Nice (France).
- Edwards, T., Maurer, G., Newman, J., Prausnitz, J., 1978. Vapor-liquid equilibria in multicomponent aqueous solutions of volatile weak electrolytes. *A.I.Ch.E. Journal* 24 (6), 966–976.
- Harvey, A., Kaplan, S., Burnett, J., 2005. Effect of dissolved air on the density and refractive index of water. *International Journal of Thermophysics* 26 (5), 1495–1514.
- Harvey, E., Smith, W., 1959. The absorption of carbon dioxide by a quiescent liquid. *Chemical Engineering Science* 10, 274–280.
- Haut, B., Halloin, V., Cartage, T., Cockx, A., 2004. Production of sodium bicarbonate in industrial bubble columns. *Chemical Engineering Science* 59, 5687–5694.
- Hecht, E., 1987. *Optics*, seconde Edition. Addison-Wesley.
- Higbie, R., 1935. The rate of absorption of pure gas into a still liquid during short periods of exposure. *Transactions on American Institute of Chemical Engineers* 31, 365.
- Itoh, K., 1982. Analysis of the phase unwrapping algorithm. *Applied Optics* 21 (14), 2470.
- Komiya, A., Maruta, K., Nakano, Y., Hashida, T., July 2008. Visualization of transient concentration field in process of carbon dioxide absorption at gas-liquid surface. In: Proceeding of the 13th International Symposium on Flow Visualisation ISFV 13 - FLUVISU 12, CD-ROM. Nice, France.
- Konstantinov, V., Maly, A., Babenko, V., 2003. Application of holographic interferometry for determining the solubility of gases in liquids. *Technical Physics Letters* 29 (7), 566 – 568.

- Kreis, T., 1986. Digital holographic interference-phase measurement using the fourier-transform method. *Journal of Optical Society of America* 3 (6), 847–855.
- Kreis, T., 2005. *Handbook of Holographic Interferometry : Optical and Digital Method*. Wiley-VCH.
- Planck, M., 1903. *Treatise on thermodynamics*. Longmans, Green, London, accd sur <http://www.archive.org/details/treatiseonthermo00planrich>. URL <http://www.archive.org/details/treatiseonthermo00planrich>
- Pohorecki, R., Moniuk, W., 1988. Kinetics of reaction between carbon dioxide and hydroxyl ions in aqueous electrolyte solutions. *Chemical Engineering Science* 43, 1677–1684.
- Schumpe, A., 1993. The estimation of gas solubilities in salt solutions. *Chemical Engineering Science* 48, 153–158.
- Taghizadeh, M., Jallut, C., Tayakout-Fayolle, M., Lieto, J., 2001. Non-isothermal gas-liquid absorption with chemical reaction studies: Temperature measurements of a spherical laminar film surface and comparison with a model for the CO₂/NaOH system. *Chemical Engineering Journal* 82, 143–148.
- Takeda, M., Ina, H., Kobayashi, S., 1982. Fourier-transform method of fringe-pattern analysis for computer-based tomography and interferometry. *J. Opt. Soc. Am.* 72 (1), 156–160.
- Trambouze, P., Euzen, J.-P., 2004. *Chemical Reactors: from design to operation*. Institut Franais du ptole publications. Technip.
- Vas Bhat, R., Kuipers, J., Versteeg, G., 2000. Mass transfer with complex chemical reactions in gas-liquid systems: two-step reversible reactions with unit stoichiometric and kinetic orders. *Chemical Engineering Journal* 10, 127–152.
- Walter, E., Pronzato, L., 1997. *Identification of parametric models from experimental data*. Springer, Berlin.
- Whitman, W., 1923. The two-film theory of absorption. *Chemistry and Metal Engineering* 29, 147.

- William W. Macy, Jr., 1983. Two-dimensional fringe-pattern analysis. *Applied Optics* 22 (23), 3898–3901.
- Wylock, C., 2009. Contribution à l'étude des transferts de matière gaz-liquide en présence de réactions chimiques. Ph.D. thesis, Université Libre de Bruxelles.
- Wylock, C., Dehaeck, S., Rednikov, A., Colinet, P., 2008. Chemo-hydrodynamic instability generated by CO₂ absorption in an aqueous solution of NaHCO₃ and Na₂CO₃. *Microgravity Science and Technology* 200, 171–175.

Table 1: Fitted values of the base parameters.

$[\text{NaHCO}_3]_0$ $\left(\frac{\text{mol}}{\text{m}^3}\right)$	$[\text{Na}_2\text{CO}_3]_0$ $\left(\frac{\text{mol}}{\text{m}^3}\right)$	$D_{\text{HCO}_3^-}$ $\left(10^{-10} \frac{\text{m}^2}{\text{s}}\right)$	$D_{\text{CO}_3^{2-}}$ $\left(10^{-10} \frac{\text{m}^2}{\text{s}}\right)$	$\frac{\partial \rho}{\partial [\text{HCO}_3^-]}$ $\left(10^{-2} \frac{\text{kg}}{\text{mol}}\right)$	$\frac{\partial \rho}{\partial [\text{CO}_3^{2-}]}$ $\left(10^{-2} \frac{\text{kg}}{\text{mol}}\right)$
246	195	9.89	9.26	5.05	10.31
246	195	7.76	7.27	5.31	10.79
256	609	4.51	4.34	5.23	10.68
256	609	4.30	4.15	5.67	11.54
266	1055	8.98	8.44	5.32	10.63
266	1055	8.97	8.36	5.34	10.64
276	1534	9.12	8.65	5.23	10.53
276	1534	3.27	3.20	5.58	11.30
282	1786	2.72	2.59	5.72	11.81
282	1786	4.16	3.67	5.74	11.82
499	198	7.44	7.27	5.30	10.66
500	198	9.10	8.80	5.33	10.70
519	617	4.63	4.51	5.83	11.71
539	1068	4.01	3.87	5.72	11.52
539	1068	11.1	11.0	5.16	10.33
559	1552	3.40	3.22	6.03	12.32
560	1553	2.89	2.58	5.60	11.38
760	201	11.4	11.1	4.96	9.99
760	201	9.58	9.09	5.25	10.49
774	409	3.55	3.42	5.95	12.04
774	409	7.53	6.98	5.66	11.41
788	625	3.62	3.41	5.37	11.09
789	625	5.25	5.05	5.52	11.13

Table 2: Fitted values of k_{11} , h and K_2 .

$[\text{NaHCO}_3]_0$ $\left(\frac{\text{mol}}{\text{m}^3}\right)$	$[\text{Na}_2\text{CO}_3]_0$ $\left(\frac{\text{mol}}{\text{m}^3}\right)$	k_{11} $\left(\frac{\text{m}^3}{\text{mols}}\right)$	h (-)	K_2 $\left(\frac{\text{m}^3}{\text{mol}}\right)$
246	195	10.44	0.64	3.88
246	195	10.22	0.63	5.37
256	609	10.71	0.51	4.38
256	609	12.82	0.45	5.24
266	1055	17.75	0.31	5.31
266	1055	17.74	0.31	5.22
276	1534	24.66	0.20	5.72
276	1534	24.55	0.21	5.47
282	1786	28.43	0.15	5.82
282	1786	29.18	0.15	5.34
499	198	9.54	0.56	5.42
500	198	10.37	0.55	5.29
519	617	13.66	0.36	5.56
539	1068	18.58	0.26	5.85
539	1068	18.56	0.27	5.31
559	1552	25.81	0.16	5.51
560	1553	27.23	0.13	4.71
760	201	10.36	0.49	5.40
760	201	10.20	0.49	4.85
774	409	11.62	0.43	4.03
774	409	12.05	0.41	5.03
788	625	14.49	0.30	5.52
789	625	13.88	0.34	5.14

List of Figures

1	Block-diagram of the interactions between the four modules. . .	33
2	Block-diagram of the experimental cell.	34
3	Schematic view of the Mach-Zehnder interferometer.	34
4	Diagram of the cell observation window (left) and example of a reference interferogram taken when no absorption takes place (right).	34
5	Interferograms before the beginning of the transfer (a) and 15 min after the beginning of the transfer (b).	35
6	Image of the logarithm of the 2-D fast Fourier transform of an interferogram (a) and image after filtering and centering (b). .	35
7	Wrapped phase shift obtained after the image processing. . . .	36
8	Refractive index variation field.	36

9	Normalized simulated concentration profiles of CO_2 , HCO_3^- and CO_3^{2-} after 15 min.	37
10	Refractive index versus density of NaHCO_3 and Na_2CO_3 aqueous solution at 20°C	37
11	Density variation field and window of averaging (a) ; density variation profiles obtained from density variation fields at several times (b).	38
12	Density versus the HCO_3^- concentration at 20°C	38
13	Density versus the CO_3^{2-} concentration at 20°C	39
14	Simulated density variation profiles 15 min after the beginning of the CO_2 absorption. $[\text{NaHCO}_3]_0 = 774 \frac{\text{mol}}{\text{m}^3}$ and $[\text{Na}_2\text{CO}_3]_0 = 409 \frac{\text{mol}}{\text{m}^3}$	39
15	Comparison of the experimental and simulated density variation profiles computed with the parameter values estimated with the literature correlations. $[\text{NaHCO}_3]_0 = 774 \frac{\text{mol}}{\text{m}^3}$ and $[\text{Na}_2\text{CO}_3]_0 = 409 \frac{\text{mol}}{\text{m}^3}$	39
16	Comparison of the experimental and simulated density variation profiles with fitted values of $D_{\text{HCO}_3^-}$, $D_{\text{CO}_3^{2-}}$, $\frac{\partial\rho}{\partial[\text{HCO}_3^-]}$, $\frac{\partial\rho}{\partial[\text{CO}_3^{2-}]}$: full profiles (a) and zoom on the zone close to the interface (b). $[\text{NaHCO}_3]_0 = 774 \frac{\text{mol}}{\text{m}^3}$ and $[\text{Na}_2\text{CO}_3]_0 = 409 \frac{\text{mol}}{\text{m}^3}$	40
17	Comparison of the experimental and simulated density variation profiles with fitted values of $D_{\text{HCO}_3^-}$, $D_{\text{CO}_3^{2-}}$, $\frac{\partial\rho}{\partial[\text{HCO}_3^-]}$, $\frac{\partial\rho}{\partial[\text{CO}_3^{2-}]}$, h , k_{11} , K_2 : full profiles (a) and zoom on the zone close to the interface (b). $[\text{NaHCO}_3]_0 = 774 \frac{\text{mol}}{\text{m}^3}$ and $[\text{Na}_2\text{CO}_3]_0 = 409 \frac{\text{mol}}{\text{m}^3}$	41

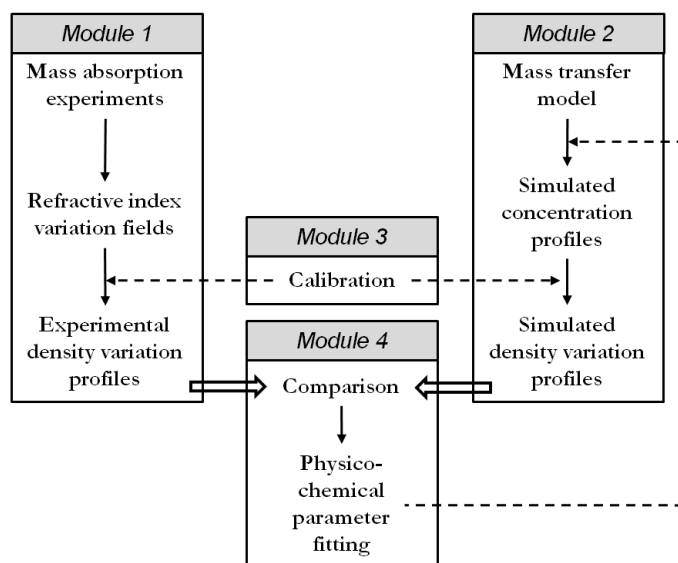


Fig. 1

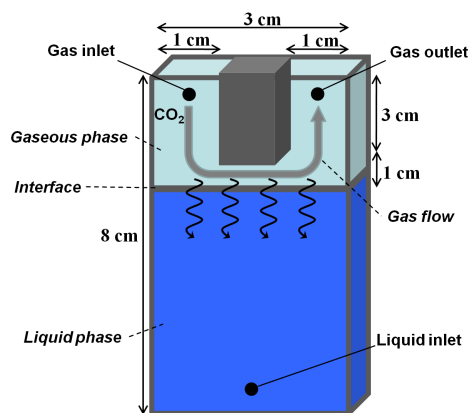


Fig. 2

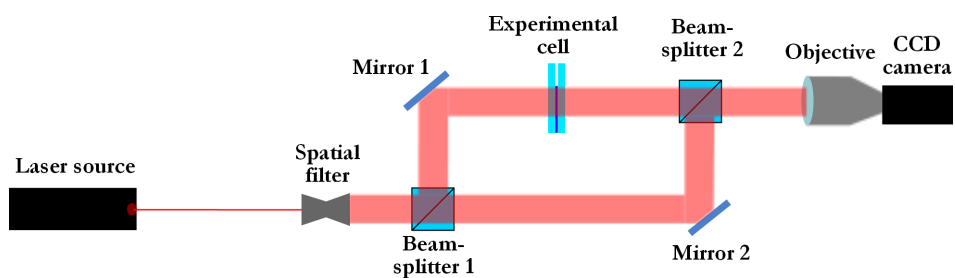


Fig. 3

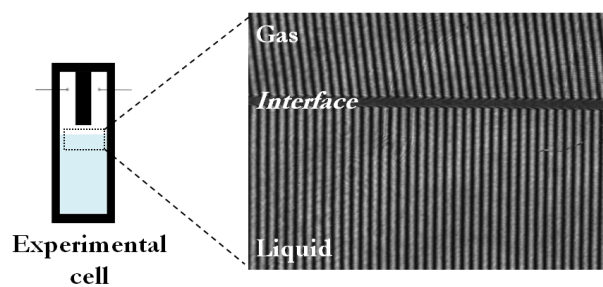


Fig. 4

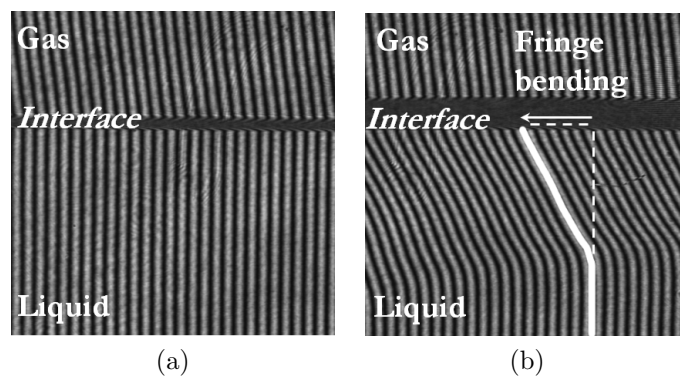


Fig. 5

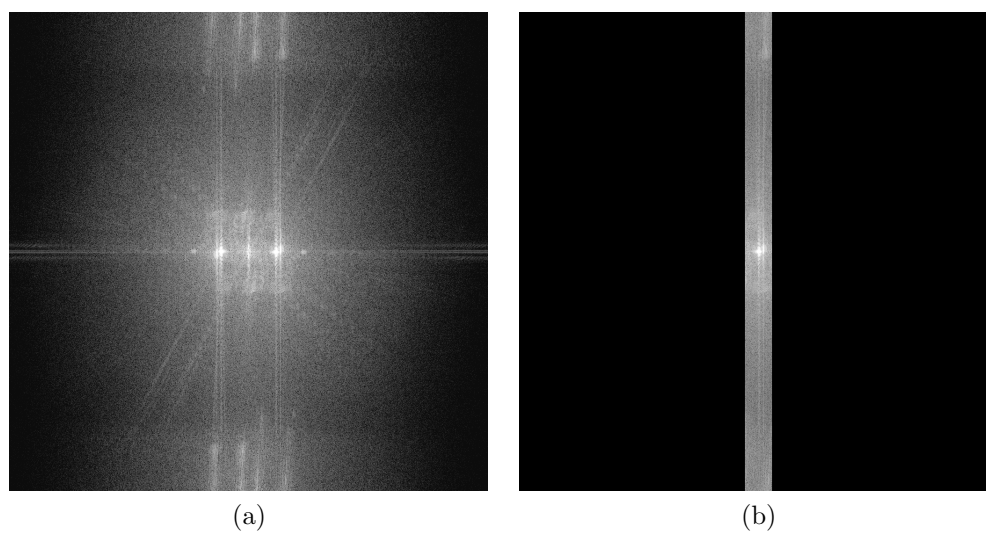


Fig. 6

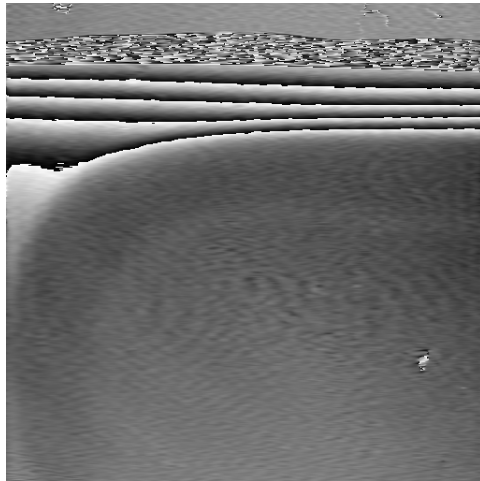


Fig. 7

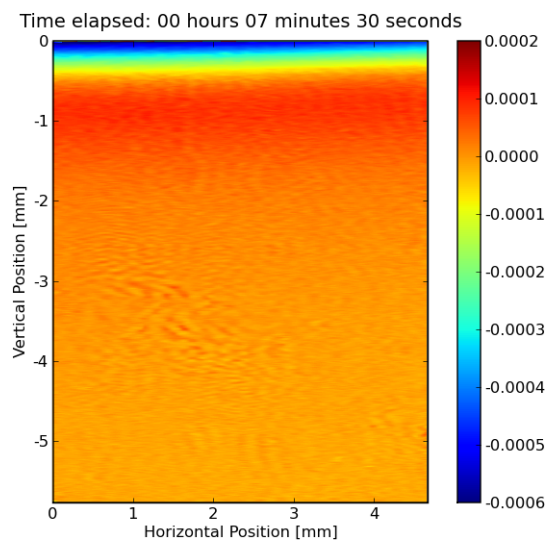


Fig. 8

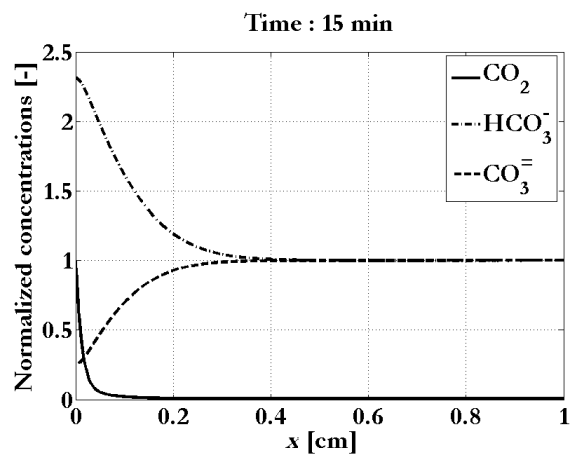


Fig. 9

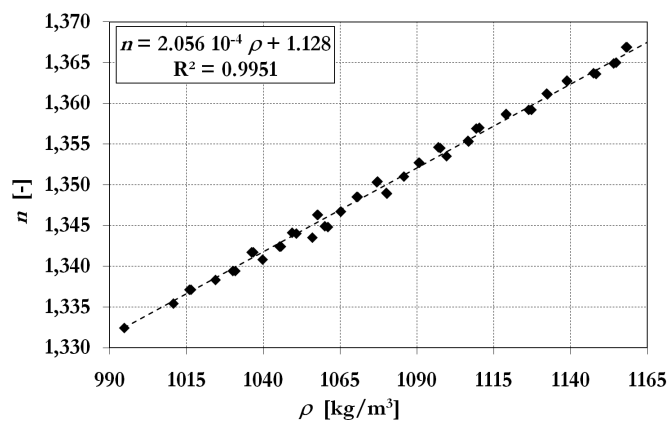


Fig. 10

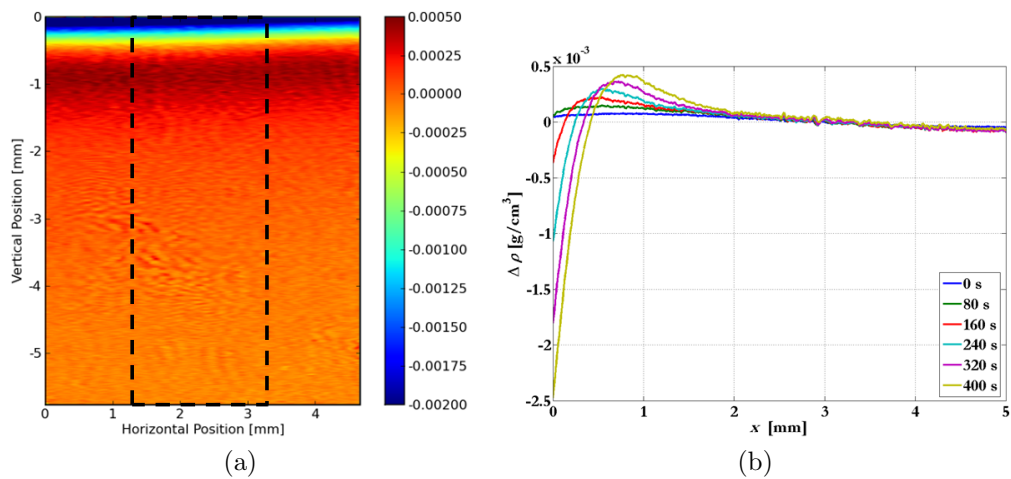


Fig. 11

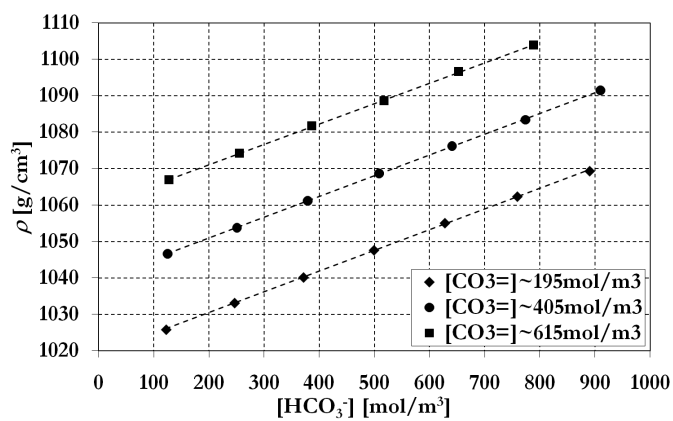


Fig. 12

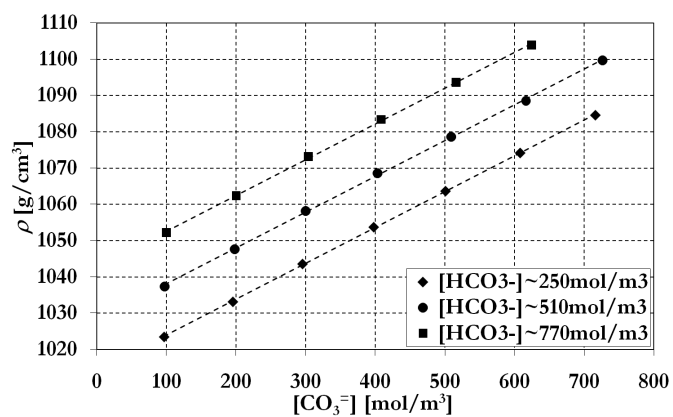


Fig. 13

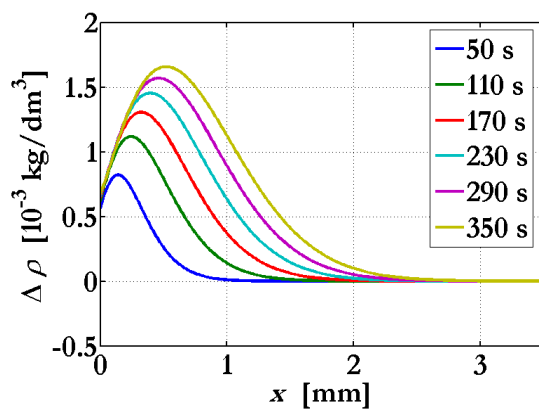


Fig. 14

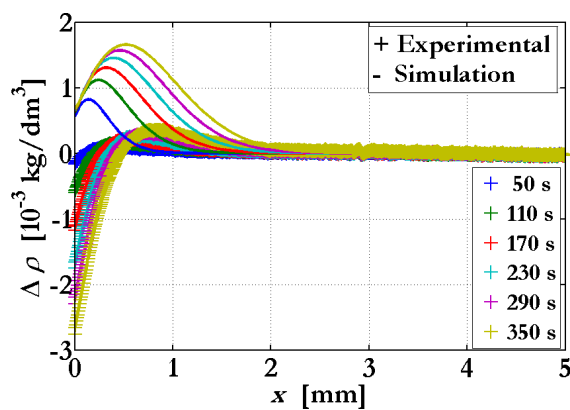
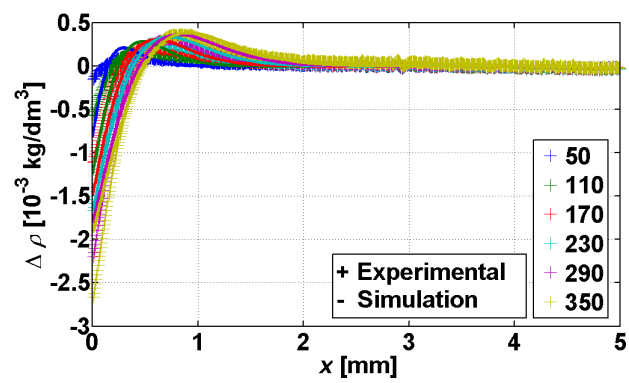
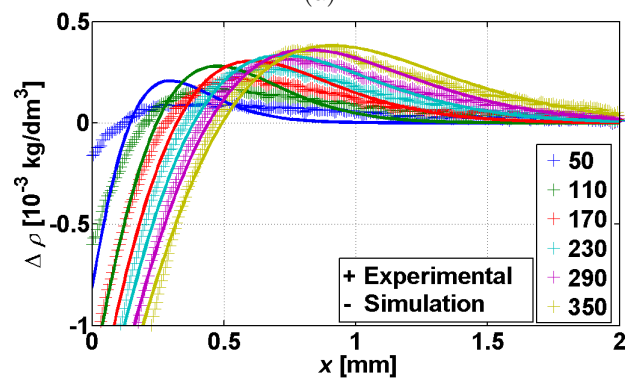


Fig. 15

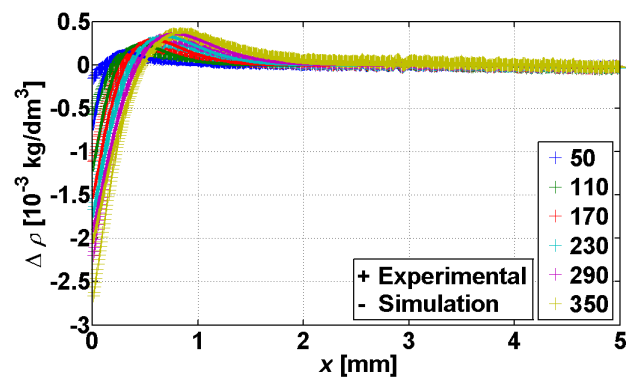


(a)

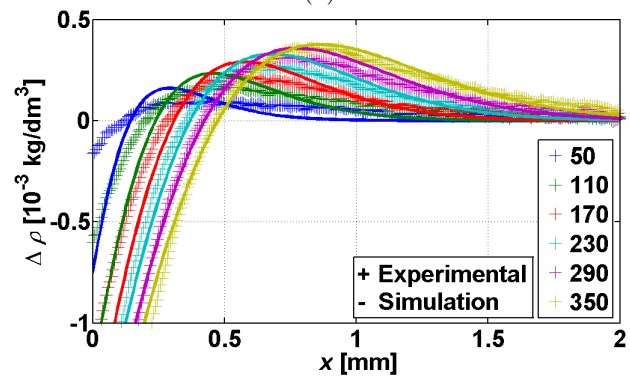


(b)

Fig. 16



(a)



(b)

Fig. 17